

Investigating the orbital evolution of the eccentric HMXB GX 301–2 using long-term X-ray light curves

Hemanth Manikantan *, Manish Kumar , Biswajit Paul and Vikram Rana 

Astronomy & Astrophysics Department, Raman Research Institute, CV Raman Avenue, Sadashivanagar, Bangalore 560080, India

Accepted 2023 October 3. Received 2023 October 3; in original form 2023 September 4

ABSTRACT

We report the orbital decay rate of the high-mass X-ray binary GX 301–2 from an analysis of its long-term X-ray light curves and pulsed flux histories from *CGRO/BATSE*, *RXTE/ASM*, *Swift/BAT*, *Fermi/GBM*, and *MAXI* by timing the pre-periastron flares over a span of almost 30 yr. The time of arrival of the pre-periastron flares exhibits an energy dependence (hard lag) and the orbital period decay was estimated after correcting for it. This method of orbital decay estimation is unaffected by the fluctuations in the spin rate of the X-ray pulsar associated with variations in the mass accretion rate. The resulting $\dot{P}_{\text{orb}} = -(1.98 \pm 0.28) \times 10^{-6} \text{ s s}^{-1}$ indicates a rapid evolution time-scale of $|P_{\text{orb}}/\dot{P}_{\text{orb}}| \sim 0.6 \times 10^5 \text{ yr}$, making it the high mass X-ray binary with the fastest orbital decay. Our estimate of \dot{P}_{orb} is off by a factor of ~ 2 from the previously reported value of $-(3.7 \pm 0.5) \times 10^{-6} \text{ s s}^{-1}$ estimated from pulsar TOA analysis. We discuss various possible mechanisms that could drive this rapid orbital decay and also suggest that GX 301–2 is a prospective Thorne–Żytkow candidate.

Key words: accretion, accretion discs – methods: data analysis – pulsars: general – X-rays: binaries – X-rays: individual: GX 301–2.

1 INTRODUCTION

Accreting high-mass X-ray binary (HMXB) pulsars that host a rotating neutron star accreting matter from a massive companion star are hypothesized to be born from the supernova explosion of the more massive star in a preliminary binary stellar system hosting two relatively massive components ($> 12 M_{\odot}$) (Tauris & Van Den Heuvel 2006, and references therein). When the mass of the companion star is over $10 M_{\odot}$, and it is of OB spectral type, they are called supergiant HMXBs (SGXBs), which account for about one-third of the known HMXB population (Tauris & Van Den Heuvel 2006). The binary orbit of SGXBs is postulated to evolve due to (i) tidal interactions, which also causes circularization of the eccentric orbit, (ii) mass transfer from companion to the neutron star by accretion, (iii) loss of mass from the binary by the stellar wind from the companion, and (iv) radiation by gravitational waves (Paul & Naik 2011, and references therein). The most accurate estimation of the orbital parameters and, thereby, the orbital evolution of accreting X-ray pulsars are obtained by measuring the time of arrival (TOA) of the stable X-ray pulses from the X-ray pulsar. This technique is called the pulse TOA analysis. The pulse TOA technique optimizes a parameter space comprising intrinsic pulse emission time stamps from the pulsar (accounting for inherent pulse period derivatives) and the binary orbit-induced arrival time-delays in order to obtain the observed TOAs of each X-ray pulse (Nagase et al. 1982). Pulse timing analysis has been extensively used to accurately estimate the orbital evolution of SGXBs like Cen X–3, SMC X–1, LMC X–4, OAO 1657–415, and

4U 1538–52 (see Paul 2017, and references therein). Orbital decay (shrinking orbit) was observed in all the HMXBs hosting a pulsar, and the estimated decay time-scale $|P_{\text{orb}}/\dot{P}_{\text{orb}}|$ varies from $\sim 10^6 \text{ yr}$ in SMC X–1, Cen X–3, LMC X–4, and 4U 1538–52 to about $\sim 10^7 \text{ yr}$ in OAO 1657–415 and 4U 1700–37 (Table 4).

GX 301–2 is a rare galactic SGXB because of the unusually eccentric ($e \sim 0.47$) binary orbit (Sato et al. 1986), which is a peculiarity of Be-HMXBs (Paul & Naik 2011), and the only SGXB known to have a hypergiant companion (Kaper et al. 1995). GX 301–2 is located $\sim 5.3 \text{ kpc}$ away on the galactic plane and hosts a $\sim 50 M_{\odot}$ hypergiant stellar companion Wray 15–977 (BP Crucis; Kaper et al. 1995) and a NS in an $\sim 41.5 \text{ d}$ long binary orbit (Sato et al. 1986). From the $H\alpha$ absorption profile in the optical spectrum, Kaper et al. (1995) estimated the mass-loss rate from Wray 15–977 by the stellar wind to be $\lesssim 10^{-5} M_{\odot} \text{ yr}^{-1}$. A peculiar feature of GX 301–2 is its pre-periastron flaring nature, which is usually explained by enhanced accretion of matter from either a dense gas stream from the companion star (Haberl 1991, Leahy & Kostka 2008) or an equatorial gas disc circumscribing Wray 15–977 (Pravdo & Ghosh 2001). Because of the pre-periastron flare, GX 301–2 exhibits variable X-ray intensity within each orbit, and the extent of the variation is energy dependent. The intensity varies by a factor of ~ 5 in 4–10 keV and ~ 12 in 15–50 keV. The wind of the companion star is clumpy (Mukherjee & Paul 2003), and it shows strong orbital phase dependent absorption column density and iron emission line (Islam & Paul 2014; Manikantan et al. 2023). The pre-periastron flaring nature and binary ephemeris of GX 301–2 were first estimated by Sato et al. (1986) by pulse TOA analysis from *SAS-3*, *Hakucho*, and *Ariel-V* observations. A similar analysis was performed by Koh et al. (1997) on the *Compton Gamma Ray Observatory (CGRO)*/Burst and

* E-mail: hemanthm@rri.res.in

Transient Source Experiment (BATSE) data, and the reported orbital elements were consistent with Sato et al. (1986). However, the orbital solution estimated by Sato et al. (1986) and Koh et al. (1997) did not show any evidence of the decay of the orbital period. Evidence for orbital decay of the binary with $\dot{P}_{\text{orb}} = -(3.7 \pm 0.5) \times 10^{-6} \text{ s s}^{-1}$ was later discovered by Doroshenko et al. (2010) using pulse TOA analysis from a long *INTEGRAL* observation (covering about 60 per cent of a binary orbit), under the assumption of a constant spin-up/down rate (\dot{P}_{spin}) of the X-ray pulsar. This is the smallest orbital decay time-scale observed in any HMXB. However, the large luminosity change of GX 301–2 along its orbital phase is most likely due to a variable mass accretion rate, and an important implication of the variable luminosity of GX 301–2 within each orbit is its effect on the spin-up rate of the pulsar. The spin-up rate of GX 301–2 is known to be correlated with the X-ray luminosity (Koh et al. 1997). Previous estimations of orbital parameters and orbital evolution (Koh et al. 1997; Doroshenko et al. 2010), however, did not consider a luminosity-dependent period derivative (Mönkkönen et al. 2020).

In this work, we use the long-term X-ray light curves of GX 301–2 available from the X-ray All-sky monitors *Rossi X-ray Timing Explorer (RXTE)*/All-sky monitor (ASM), *Neil Gehrels Swift Observatory (Swift)*/Burst Alert Telescope (BAT) and *Monitor of All-sky X-ray Image (MAXI)* and the pulsed flux histories available from *CGRO/BATSE* and *Fermi Gamma-ray Space Telescope (Fermi)*/Gamma Burst Monitor (GBM) to investigate the orbital decay, which has previously been reported from pulse TOA analysis. Instead of the pulsar time stamps, which are used in the pulse TOA analysis, we make use of the similarity in the shapes of recurring orbital intensity profiles and the timing signature of the recurring pre-periastron flares of GX 301–2. Assuming the orbital intensity profile of GX 301–2 to preserve an overall shape over the long term, epoch folding the long-term light curves and pulsed-flux histories could be used to estimate the orbital period and period derivative. Assuming that the physical mechanism responsible for the pre-periastron flares remains stable over the long term, we also utilize the variations in the arrival times of pre-periastron flares over an extended period to estimate the rate of change of the orbital period.

2 INSTRUMENT AND OBSERVATIONS

The orbital period of GX 301–2 is relatively long, spanning 41.5 d (3586 ks), which makes conducting pointed observations throughout the entire orbit of GX 301–2 infeasible. However, being one of the brightest sources in the X-ray sky, GX 301–2 is monitored by all of the X-ray all-sky monitor observatories. The long-term light curves or pulsed flux histories from these observatories are available for over three decades.

The BATSE instrument onboard the *CGRO* (Meegan et al. 1992) consisted of eight inorganic NaI-based Scintillation detectors detecting hard X-ray photons from different parts of the sky in 20 keV–2 MeV. *CGRO/BATSE* was operational from 1991 to 2000. The pulse periods of several X-ray pulsars were measured by epoch folding technique, and their pulse period and pulsed flux histories are available for download at the BATSE Pulsars webpage.¹

The ASM onboard the *RXTE* (Jahoda et al. 1996; Levine et al. 1996) consisted of three position-sensitive Xenon proportional counters coupled to three coded-aperture masks, respectively, and it operated in the 1.5–12 keV energy band. It had a total collecting area of 90 cm² and covered almost 80 per cent of the entire sky during

each 90 min orbit, and it provided continuous data coverage of bright X-ray sources from 1996 to 2011.

The BAT onboard the Neil Gehrels Swift Observatory (Gehrels et al. 2004; Barthelmy et al. 2005) is a hard X-ray all-sky monitor operating in the 15–50 keV band. BAT consists of Cadmium Zinc Telluride (CZT) detectors (total detector area of about 5200 cm²) coupled to a 2D coded-aperture mask. This facilitates imaging of the X-ray sky with a large instantaneous field of view of 1.4 std. *Swift/BAT* has been operational since 2004.

The GBM onboard the *Fermi Gamma-ray Space Telescope* is a hard X-ray monitor operating in 8 keV–40 MeV. It consists of 12 Thallium activated Sodium Iodide (NaI(Tl)) scintillation detectors operating in 8 keV–1 MeV range and two Bismuth Germanate (BGO) scintillation detectors operating in 200 keV–40 MeV range. The GBM Accreting Pulsars Program (GAPP) provides the pulsed flux histories of bright X-ray pulsars (see Malacaria et al. 2020 for a review). It is operational since 2008.

The Gas Slit Camera (GSC) onboard the *MAXI* observatory (Matsuoka et al. 2009; Mihara et al. 2011) is an All-sky monitor onboard the International Space Station (ISS) operating in the range 2–30 keV. GSC comprises twelve large-area position-sensitive proportional counters, each coupled to a slit-slat collimator. They have an instantaneous FOV of 160° × 3° and scan the whole sky during each orbit of the ISS. The narrow FOV and position-sensitive proportional counters facilitate imaging of the X-ray sky. The long-term light curves of X-ray sources from *MAXI* are available since 2008.

We downloaded the orbit-by-orbit (dwell) long-term light curves from *RXTE/ASM* (1.5–12 keV), *Swift/BAT* (15–50 keV) and *MAXI* (2–4, 4–10, 10–20 keV). The dwell light curves have a bin size of about 90 minutes (0.0625 days). However, the pulsed flux histories from *CGRO/BATSE* and *Fermi/GBM* were available with a bin size of 1 day and 2 days, respectively. The *Swift/BAT* light curve was screened such that the data points having a value of error greater than 500 times the lowest error were excluded from the analysis.

3 ANALYSIS

We performed three independent analyses to search for the orbital period decay in GX 301–2. In the first approach, epoch folding search (Leahy 1987) was run on each long-term light curve without \dot{P}_{orb} , and the slope of the best-fitting straight line on the best periods derived from each of them as a function of time was estimated. In the second approach, epoch folding search was run on each long-term light curve for a prospective range of \dot{P}_{orb} from -3×10^{-5} to $+3 \times 10^{-5} \text{ s s}^{-1}$ to check if there is improved detection of periodicity corresponding to any \dot{P}_{orb} . This would indicate the presence of any period evolution in the long-term light curves. In the third approach, we used the times of the periodic pre-periastron flares to estimate the orbital period decay. The first two approaches depend on the long-term consistency of the orbital intensity profile of GX 301–2, which is dominated by the pre-periastron flare. The second approach depends on precisely locating the peak of the pre-periastron flares and the long-term stability of the time of arrival of pre-periastron flares. This means that the most significant factor affecting all three analyses is the accuracy of the shape of the flare. Since the flare is about 2 days long, the light curves used for analysis should preferably have a finer time resolution to construct the shape of the flare accurately. For this purpose, the 0.0625 d bin size dwell light curves were used for the analysis. However, the pulsed flux histories from BATSE and GBM were only available with a bin size of 1 d and 2 d, respectively, impacting the estimation accuracy from these two light curves.

¹<https://gammaray.nstc.nasa.gov/batse/pulsar/>

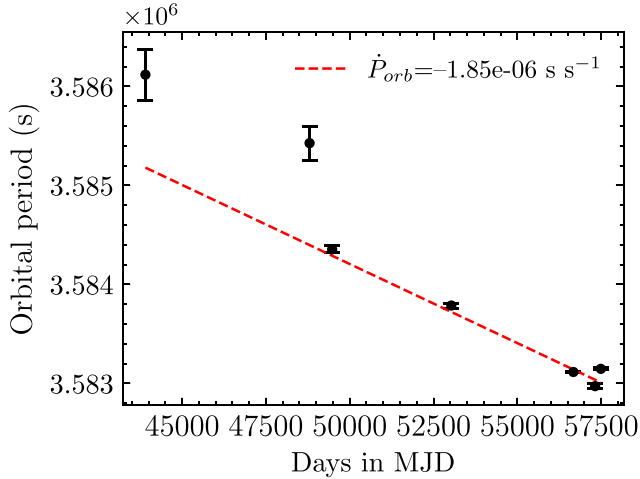


Figure 1. Estimates of the orbital periods from the long-term light curves and pulsed flux histories. \dot{P}_{orb} from fitting a linear model is $-(1.85 \pm 0.34) \times 10^{-6} \text{ s s}^{-1}$.

3.1 Epoch folding search

We ran the epoch folding search over the entire duration of each of the three long-term light curves and two pulsed flux histories mentioned in Section 2 (also see Table 2 and Fig. 4) using the HEASOFT tool *efsearch*.² We searched for periods in the vicinity of 3 583 780 s (41.5 d), which is the known binary orbital period. For estimating the error in the best period returned by *efsearch* in a light curve, we simulated 1000 instances of that particular light curve and ran *efsearch* on each of them, and the variance of the distribution of the best periods returned from 1000 light curves was used to estimate the 1σ error in the period (see Appendix A for details). The best period returned from each light curve was then assigned to the middle of the respective light curve duration and then plotted (Fig. 1 and Table 1). There is a clear trend of decreasing period, and a linear fit returned a best-fit orbital decay rate of $-(1.85 \pm 0.34) \times 10^{-6} \text{ s s}^{-1}$. The orbital profiles obtained by folding each light curve with the respective orbital periods obtained with *efsearch* are shown in Fig. 2.

3.2 Epoch folding search with a period derivative

To search for the presence of such an orbital period decay within the duration of each light curve, we ran *efsearch* with a range of sample period derivatives ranging from -3×10^{-5} to $+3 \times 10^{-5} \text{ s s}^{-1}$ on each of the light curves. The results are shown in Fig. 3. *Swift*/BAT, *Fermi*/GBM, and *MAXI* clearly show the presence of an orbital decay rate of around $-10^{-6} \text{ s s}^{-1}$ and *RXTE*/ASM is consistent with this value (see the caption of Fig. 3). However, such an orbital decay is not detected with *CGRO*/BATSE.

3.3 O–C curves using the pre-periastron flares

The recurring pre-periastron flares at regular intervals are a peculiarity of GX 301–2, and the time stamps (T_{flare}) of pre-periastron flare peaks are useful markers to track the evolution of the binary orbital period. For a stable binary orbital period without temporal evolution, if the timestamp of flare in 0th orbit (T_0) is known, the time stamp of flare in n^{th} orbit will follow the linear function

$T_0 + nP_{\text{orb}}$. Any deviation from linearity in the observed time stamps of the flares indicates orbital period evolution. The difference between the observed and computed time of flares as a function of orbit cycle number is called the O–C curve. This technique was utilized for the estimation of orbital evolution by monitoring the time of arrivals of minima in the orbital intensity profile of Cyg X–3 (Singh et al. 2002) and by tracking the mid-eclipse times of eclipsing binaries Cen X–3, SMC X–1 (Raichur & Paul 2010), and LMC X–4 (Naik & Paul 2004). We used the same technique, with the orbital-intensity minima or mid-eclipse time substituted by pre-periastron flare peak (essentially the orbital-intensity maxima).

Since the photon statistics do not allow an accurate estimation of flare times for every orbital cycle from the long-term light curves, we constructed a representative flare peak time for short-duration segments of the long-term light curves. We divided each of the five light curves into three segments of equal duration and determined a representative time of arrival of the flare in each of those time segments. The time of arrival of the flare on n^{th} orbital cycle could be expressed as a Taylor polynomial function of n :

$$T_n = T_0 + \frac{n}{1!} P_{\text{orb}} + \frac{n^2}{2!} P_{\text{orb}} \dot{P}_{\text{orb}} + \dots \quad (1)$$

T_n is the time stamp of the n^{th} pre-periastron flare peak, T_0 is the time stamp of the reference pre-periastron flare peak, P_{orb} is the orbital period, and \dot{P}_{orb} is the rate of change of orbital period. Assuming \dot{P}_{orb} is present and ignoring the higher order derivatives, equation (1) can be used to verify the presence and get an estimate of \dot{P}_{orb} if it exists (See Klis & Bonnet-Bidaud 1984; Raichur & Paul 2010).

However, the five long-term light curves are from different energy ranges, and the periodic pre-periastron flares of GX 301–2 are known to exhibit a hard X-ray lag of about a day (Liu 2020). Therefore, we checked the simultaneity of the flare peaks in the long-term light curves before proceeding with the \dot{P}_{orb} estimation. The long-term light curves and pulsed histories have overlapping data duration (see Table 2 and the vertical dashed lines in Fig. 4). We checked the flares in BATSE (20–50 keV), ASM (1.5–12 keV), BAT (15–50 keV), GBM (12–50 keV), and *MAXI* (4–10, 10–20 keV). The long-term light curve from *Swift*/BAT has considerable overlapping data duration with *RXTE*/ASM, *Fermi*/GBM, and *MAXI* light curves, and *CGRO*/BATSE has overlap with *RXTE*/ASM to perform this study. We estimated the difference in flare times (ΔT_{flare}) between light curves in the overlapping durations using the technique described in Appendix B. Except for BATSE and GBM, we found a very clear hard X-ray lag of ~ 0.9 d (Table 2). As the BATSE and GBM pulsed flux histories are generated by integrating the pulsed flux over durations of one day and two days, respectively, which is of the same order as the flare duration, it could impact the accurate construction of the flare shape and, subsequently, our estimation of the flare peak. This inadequacy of the data most likely causes the contrasting results from BATSE and GBM. We derived error scaling factors for the flare times T_n for BATSE (4.3), GBM (5.8), and *MAXI* 10–20 keV (4.0), and a time shift for ASM (+0.96 d) so that the energy dependence of flare arrival times are eliminated and all the flare times are consistent with BAT.

The time stamps of the pre-periastron flare T_n s derived from the long-term light curves were corrected for the energy dependence mentioned before and the energy independent flare times were used for further analysis. In addition to these data points, we used the flare time from Sato et al. (1986), which was derived from *Ariel-V* (2–15 keV), *SAS-3* (8–18 keV), *Hakucho* (9–22 keV), and *HEAO-1*

²<https://heasarc.gsfc.nasa.gov/ftools/fhelp/efsearch.txt>

Table 1. Estimates of the orbital period from the long-term All sky monitor light curves and pulsed flux history light curves with associated 1σ error bars.

Observatory	Epoch (MJD)	Best period (s)	Reference
<i>SAS-3</i> , <i>Hakucho</i> , <i>Ariel-V</i> ^a	43906.06	3586291.2 ± 604.8	Sato et al. (1986)
<i>INTEGRAL</i> ^a	43906.06	3586118.4 ± 259.2	Doroshenko et al. (2010)
<i>CGRO/BATSE</i> ^a	48802.79	3585427.2 ± 172.8	Koh et al. (1997)
<i>CGRO/BATSE</i>	49475.00	3584355.24 ± 36.34	This work
<i>RXTE/ASM</i> ^b	53030.00	3583787.19 ± 24.95	This work
<i>Swift/BAT</i>	56671.32	3583115.88 ± 3.92	This work
<i>Fermi/GBM</i>	57318.77	3582973.00 ± 22.67	This work
<i>MAXI</i>	57489.84	3583147.78 ± 9.45	This work

^aFrom pulse TOA analysis. ^b1.5–12 keV band.

The long-term light curves from *RXTE/ASM*, *Swift/BAT*, and *MAXI* have bin size of 0.0625 d. The pulsed flux history from *CGRO/BATSE* and *Fermi/GBM* have bin sizes of 1.0 and 2.0 d, respectively.

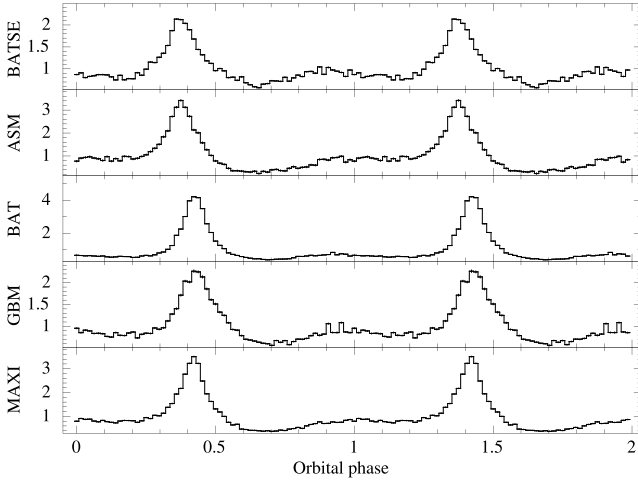


Figure 2. The orbital profiles of GX 301–2 obtained by folding the long-term light curves. The y-axis has units of cts s^{-1} normalized by the average source count rate (normalized intensity). The light curves were folded at an epoch MJD 48370.5 corresponding to the beginning of BATSE light curve with the orbital periods derived from respective light curves (Table 1).

(15–175 keV). The T_n vs n was then fitted with a linear function in n (mimicking $T_0 + nP_{\text{orb}}$), and the residuals to the linear fit (δT_n or O–C vs n) were plotted. A clear negative parabolic trend was visible in the residuals, indicating the orbital decay (Fig. 5). Fitting a function of the form $T_0 + nP_{\text{orb}} + 0.5n^2P_{\text{orb}}\dot{P}_{\text{orb}}$ gave the best fit \dot{P}_{orb} as $-(1.93 \pm 0.11) \times 10^{-6} \text{ s s}^{-1}$ (Fig. 5 top). However, the fit-statistic was large, and we, therefore, scaled the errors on flare times by a factor of 3. This is justified because, along with the regular pre-periastron flares, GX 301–2 is also known to exhibit short-term variability, which could contribute to additional systematic error in the determination of pre-periastron flare times. Scaling of errors improved the fit statistic and the subsequently obtained best fit \dot{P}_{orb} is $-(1.98 \pm 0.28) \times 10^{-6} \text{ s s}^{-1}$ (Fig. 5 bottom).

4 DISCUSSIONS

4.1 Estimation of decay in orbital period

The rapid orbital decay rate of GX 301–2 was estimated by Doroshenko et al. (2010) from multiple *INTEGRAL* pointed observations by timing the X-ray pulses. A constant \dot{P}_{spin} of the pulsar

was assumed in the calculation. However, GX 301–2 exhibits an intensity variation by a factor of 15 within the orbit (evident from folded *Swift/BAT* orbital intensity profile in Fig. 2) and even a factor of 3 during the out-of-flare states (Fürst et al. 2018). The torque state of the X-ray pulsar is also known to be dependent on its luminosity (Pravdo & Ghosh 2001). These factors adversely impact the assumption of a constant \dot{P}_{spin} and subsequently the estimation of \dot{P}_{orb} (Mönkkönen et al. 2020).

Our estimate of the orbital period decay from an independent method using the flare timing signatures in long-term X-ray light curves is not affected by the uncertainty of \dot{P}_{spin} . Assuming the individual flare peaks are accurate to $\delta t \sim 0.0625 \text{ d}$, for a time interval of $\Delta t \sim 10^4 \text{ d}$, an orbital evolution time-scale $|t_p| = |P_{\text{orb}}/\dot{P}_{\text{orb}}| \sim 10^5 \text{ yr}$ could be estimated to a precision of $t_p \delta t / \Delta t^2 \times 100 \sim 2$ per cent (Eggleton 2006). However, this technique of \dot{P}_{orb} estimation will depend on the shape of the orbital intensity profile, which has the major contribution from the pre-periastron flare and will be the main contributor to the uncertainty of this technique. Even though not entirely understood, the orbital profile of GX 301–2 is generally explained on the basis of two common models by (i) Pravdo & Ghosh (2001) based on an equatorial circumstellar disc of gas around the companion star and (ii) Haberl (1991); Leahy & Kostka (2008) based on a dense stream of matter from the companion following the pulsar. Changes in the properties of the circumstellar disc or the accretion stream could therefore result in variations in the shape of the orbital intensity profile. Our analysis is the most accurate if the orbital intensity profile stays the same throughout the long-term data used for the analysis.

Our analysis also suggests the presence of a rapid orbital decay. The estimate of orbital period decay is $\dot{P}_{\text{orb}} = -(1.98 \pm 0.28) \times 10^{-6} \text{ s s}^{-1}$ corresponding to an orbital evolution time-scale of $|P_{\text{orb}}/\dot{P}_{\text{orb}}| \approx 0.6 \times 10^5 \text{ yr}$. Our estimate of \dot{P}_{orb} is different from the value reported by Doroshenko et al. (2010), which is $-(3.7 \pm 0.5) \times 10^{-6} \text{ s s}^{-1}$, by a factor of ~ 2 .

4.2 Possible reasons for the rapid orbital decay

The observed orbital evolution time-scale of $|P_{\text{orb}}/\dot{P}_{\text{orb}}| \sim 10^5 \text{ yr}$ in GX 301–2 is an order of magnitude shorter than the mass-loss time-scale of the companion of $|M_c/\dot{M}_c| \sim 10^6 \text{ yr}$. Until now, this is the fastest orbital decay ever observed in an HMXB (see Table 4). Even though there was a recent report by Shirke et al. (2021) of a much larger orbital decay rate of $|\dot{P}_{\text{orb}}/P_{\text{orb}}| \sim 10^{-4} \text{ yr}^{-1}$ in the HMXB Cen X–3, which contradicts previous measurements (Table 4), it should be noted that for the pulse TOA analysis, the authors utilized data from only a portion (half) of one orbit, and any intrinsic variations

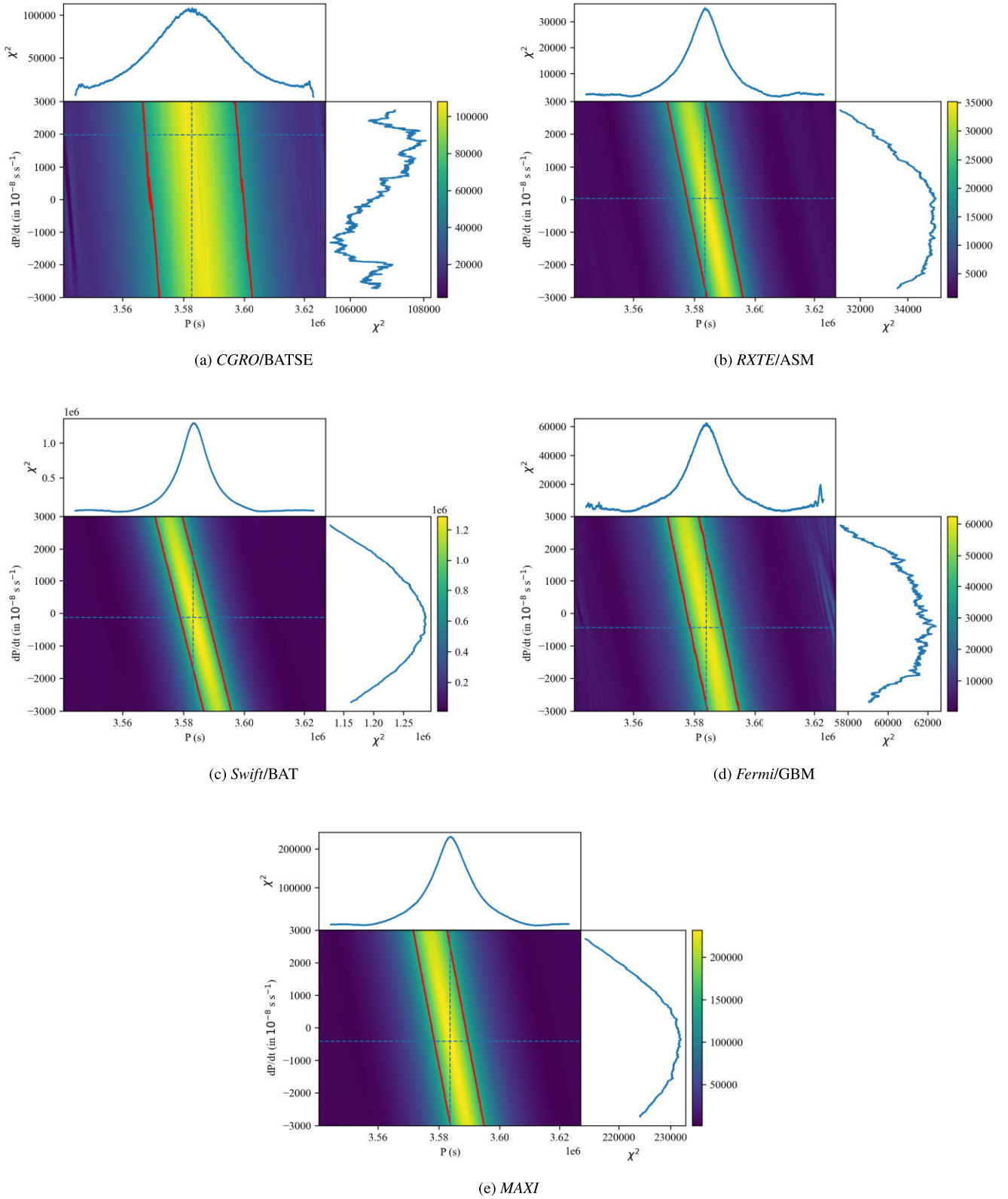


Figure 3. Figure shows the results of *efsearch* for different \dot{P} values, when run on three long-term light curves and two pulsed flux histories. The epoch used for the period search for each light curve is the start of the respective light curve. Each plot has three panels, and the middle panel has $\chi^2 - P$ horizontal plots stacked vertically for different values of \dot{P} , with χ^2 colour coded. The top panel shows the $\chi^2 - P$ plot returned for the best \dot{P} ($\chi^2 - P$ with the highest χ^2_{peak}), and the right panel shows the χ^2_{peak} obtained from each *efsearch* run with a particular \dot{P} . The pair of horizontal and vertical dashed lines in the middle panel denotes (P , \dot{P}) corresponding to the highest χ^2_{peak} along each axes. *Swift/BAT*, *MAXI*, and *Fermi/GBM* show the presence of a secular \dot{P}_{orb} of the order of 10^{-6} s s^{-1} , and *RXTE/ASM* is consistent with such a value, but such a trend is not evident in *CGRO/BATSE*.

Table 2. The difference in time of arrivals of the pre-periastron flare in different energy bands estimated from overlapping duration of the long-term light curves.

Observatory/Instrument	Energy range (keV)	LC duration (MJD)	No. of orbits during overlap	ΔT_{flare} (d)
<i>CGRO</i> /BATSE	20–50 keV	48370–50579	Reference LC	
<i>RXTE</i> /ASM	1.5–12 keV	50133–55927	10	-0.57 ± 0.09
<i>Swift</i> /BAT	15–50 keV	53416–59927	Reference LC	
<i>RXTE</i> /ASM	1.5–12 keV	50133–55927	60	-0.96 ± 0.06
<i>Fermi</i> /GBM	12–50 keV	54691–59947	126	-0.23 ± 0.04
<i>MAXI</i>	2–20 keV	55053–59927	116	-0.36 ± 0.02
	4–10 keV	''	''	-0.88 ± 0.03
	10–20 keV	''	''	-0.08 ± 0.02

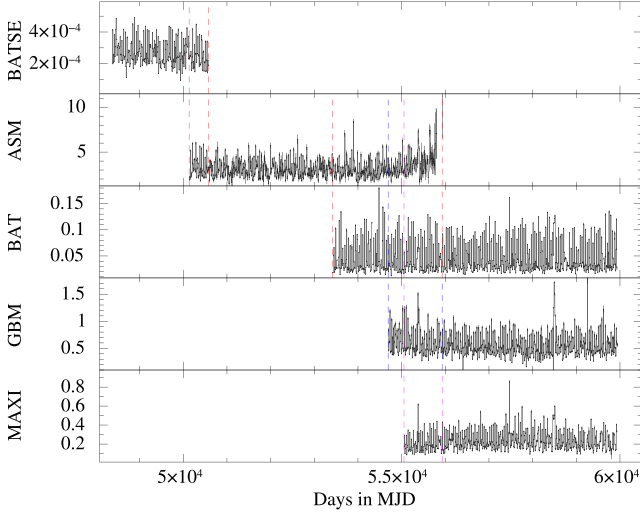


Figure 4. The long-term light curves and pulsed flux histories from different All-sky monitors plotted with a bin size of 10 d. The overlapping duration for BATSE–ASM, BAT–ASM, BAT–GBM and BAT–MAXI are represented with vertical dashed lines. The simultaneous data allowed a check for the energy dependence of flares, and we found a clear hard lag (Table 2).

in the pulsar spin rate may have contributed to this disparate result. Disregarding this report, GX 301–2 has exhibited the fastest observed orbital decay among HMXBs, and we are examining potential causes for the observed orbital decay.

The orbital evolution of a binary star system can be described by the changes in its orbital angular momentum and mass transfer (Tauris & Van Den Heuvel 2006; Bachetti et al. 2022) as follows:

$$\frac{2}{3} \frac{\dot{P}_{\text{orb}}}{P_{\text{orb}}} = 2 \frac{\dot{J}_{\text{orb}}}{J_{\text{orb}}} - 2 \frac{\dot{M}_c}{M_c} - 2 \frac{\dot{M}_x}{M_x} + \frac{\dot{M}_c + \dot{M}_x}{M_c + M_x} - 2e\dot{e}. \quad (2)$$

In equation (2), the binary orbital period P_{orb} and its rate of change \dot{P}_{orb} are expressed in terms of the evolution of other binary parameters. J_{orb} and \dot{J}_{orb} are the orbital angular momentum of the binary and its rate of change, respectively, M_c and \dot{M}_c are the companion mass and its rate of change, respectively, and M_x and \dot{M}_x are the NS mass and its rate of change, respectively.

Some of these parameters are known for GX 301–2 (Table 3). The observed orbital decay ($\dot{P}_{\text{orb}} < 0$) in GX 301–2 could be investigated through equation (2), which implies that $\dot{J}_{\text{orb}} < 0$, $\dot{e} > 0$ and certain combinations of \dot{M}_c , \dot{M}_x , M_x , and M_c has the potential to cause $\dot{P}_{\text{orb}} < 0$. Furthermore, some of these parameters may exert a greater influence on \dot{P}_{orb} compared to the others. A case in point is, although equation (2) suggests that $\dot{e} < 0$ can lead to the expansion of the orbit, the opposite is observed in HMXBs. The reason could be that $\dot{e} < 0$

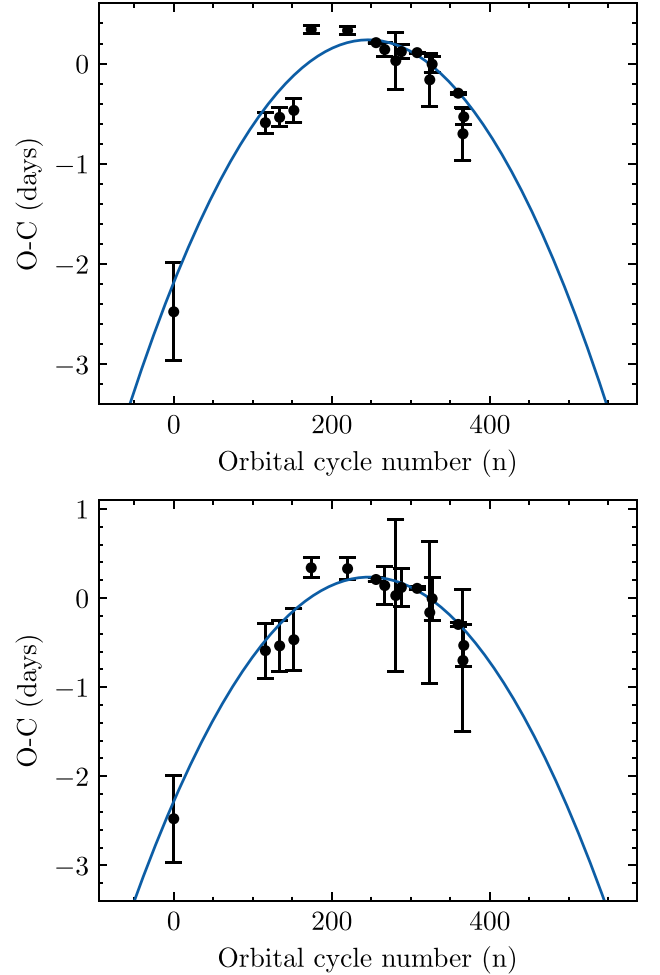


Figure 5. O–C curve from the pre-periastron flare peak times derived from BATSE, ASM, BAT, GBM, and MAXI. The first data point is taken from Sato et al. (1986). Errors in the BATSE, GBM, and MAXI data points were scaled by factors of 4.3, 5.8, and 4.0, respectively, and the ASM data points were shifted by +0.96 d to account for the energy dependence of flare times (see text). Top figure shows the quadratic fit indicating $\dot{P}_{\text{orb}} = -(1.93 \pm 0.11) \times 10^{-6} \text{ s}^{-1}$. However, the weighted variance (wvar) of the fit was poor at 145 for 14 (16 – 3 + 1) d.o.f, which impacts the parameter error estimation. The large variance was contributed by the low error bar of the data points ($\sum_{i=1}^{15} (\frac{d_i - m_i}{e_i})^2 \sim 145$). To make the wvar \approx d.o.f, we scaled up each error e_i with a scaling factor of $\sqrt{145/15} \sim 3$. This reduced the wvar to ~ 16 (14 d.o.f). The bottom figure shows the best-fitting quadratic model on the error re-scaled data. Best-fitting \dot{P}_{orb} is $-(1.98 \pm 0.28) \times 10^{-6} \text{ s}^{-1}$. The quoted errors on all the parameters are their 2.7σ confidence ranges.

Table 3. Some reported estimates of GX 301–2 parameters. We used these values to assess various possible reasons driving the observed orbital decay in GX 301–2 in Section 4.2.

Parameter	Value	Reference
P_{orb}	41.5 d	Sato et al. (1986)
$ \dot{P}_{\text{orb}}/P_{\text{orb}} $	$5.52 \times 10^{-13} \text{ s}^{-1}$ $1.74 \times 10^{-5} \text{ yr}^{-1}$	This work
M_x	$1.4 M_{\odot}$	Canonical
M_c	$50 M_{\odot}$	Kaper et al. (1995)
R_c	$87 R_{\odot}$	Kaper et al. (1995)
i	$\leq 64^{\circ}$	Kaper et al. (1995)
$a_x \sin i$	$159 \pm 1.5 R_{\odot}$	Sato et al. (1986)
a_x	$177 R_{\odot}$	
e	0.47	Sato et al. (1986)
\dot{M}_c	$-(3 \text{ to } 10) \times 10^{-6} M_{\odot} \text{ yr}^{-1}$	Parkes et al. (1980); Kaper et al. (1995)
v_{wind}	400 km s^{-1}	Parkes et al. (1980)
$v_e \sin i$	55 km s^{-1}	Clark et al. (2012)
v_e	61 km s^{-1}	
P_c^{\dagger}	72 d	

$$\dagger P_c = 2\pi R_c / v_e.$$

Table 4. Previous reports of the orbital decay reported for HMXBs in the order of increasing $|\dot{P}_{\text{orb}}/P_{\text{orb}}|$. The evolution time-scale is of the order of the inverse of the second column. The shortest evolution time-scale corresponds to GX 301–2 ($\sim 10^5$ yr), and the longest evolution time-scale corresponds to OAO 1657–415 ($\sim 10^7$ yr).

Source	$\dot{P}_{\text{orb}}/P_{\text{orb}}$ (in 10^{-6} yr^{-1})	Reference
OAO 1657–415	-0.0974 ± 0.0078	Jenke et al. (2012)
4U 1700–37	-0.47 ± 0.19	Islam & Paul (2016)
4U 1538–52	-0.95 ± 0.37	Hemphill et al. (2019)
Cyg X–3	-1.05 ± 0.04	Singh et al. (2002)
LMC X–4	-0.989 ± 0.005	Naik & Paul (2004)
Cen X–3	-1.799 ± 0.002	Raichur & Paul (2010)
SMC X–1	-3.414 ± 0.003	Raichur & Paul (2010)
GX 301–2	-32.5 ± 4.4 -17.4 ± 2.5	Doroshenko et al. (2010) This work

in HMXBs arises from tidal interactions, which also results in $\dot{J}_{\text{orb}} < 0$ and the \dot{J} term dominates over the \dot{e} term, causing the orbit to decay instead of expanding.

Our aim is to evaluate three feasible factors that could produce the observed orbital decay in GX 301–2, which are mass transfer from the companion to the NS, mass-loss from the binary, and tidal interaction between NS and the companion. The conservation of J_{orb} characterizes the former mechanism, in which the decay of the orbit is driven by mass redistribution. On the other hand, the latter two mechanisms are characterized by loss of J_{orb} , leading to the decay of the orbit. Recent simulations of GX 301–2 by Bunzel et al. (2023) do not predict this rapid orbital decay before the Common Envelope phase, but not all of the aforementioned mechanisms were included in their simulations. Although the loss of J_{orb} is also possible due to gravitational wave radiation and magnetic braking, they are only dominant in orbits that are sufficiently compact (van den Heuvel 1994), and hence we do not discuss it further.

4.2.1 Conservative mass transfer

The simplest case is the conservative mass transfer from companion to the NS, where the orbital angular momentum is conserved ($\dot{J}_{\text{orb}} = 0$), and eccentricity stays constant ($\dot{e} = 0$). In the scenario of

conservative mass transfer, the entire mass lost by the companion is accreted by the neutron star ($-\dot{M}_c = \dot{M}_x$), and there is no significant alteration of the orbital angular momentum ($\dot{J}_{\text{orb}} = 0$).

Substituting the values from Table 3 in equation (1), the required mass transfer rate (accretion rate) to the NS for attaining the observed orbital decay rate is $\dot{M}_x \sim 8 \times 10^{-6} M_{\odot} \text{ yr}^{-1}$. This is roughly the mass-loss rate from the companion (Table 3). However, the Eddington accretion limit for spherical accretion of hydrogen-rich matter to a canonical $1.4 M_{\odot}$ 10 km radius NS is about $10^{-8} M_{\odot} \text{ yr}^{-1}$ (van den Heuvel 1994), implying only a maximum of ~ 1 per cent of the mass lost by Wray 15–977 could be accreted by the NS even if it is accreting at the Eddington limit. Therefore, conservative mass transfer can't be the primary mechanism driving the observed \dot{P}_{orb} in GX 301–2.

4.2.2 Mass-loss from the binary

The efficiency of wind accretion in GX 301–2 could be calculated using the equations $e_{\text{wind}} = \pi r_{\text{acc}}^2 / 4\pi a_x^2$ and $r_{\text{acc}} = GM_x / v_w^2$. Here, e_{wind} is the efficiency of wind accretion, v_w is the velocity of stellar wind from the companion, and accretion radius r_{acc} is the distance from the NS at which the stellar wind is gravitationally captured. Substituting values for GX 301–2 from Table 3 gives the efficiency of wind accretion $e_{\text{wind}} \sim 3 \times 10^{-5}$. The unaccreted matter will likely be lost from the binary and contribute to \dot{J}_{orb} . A complete consideration of mass-loss from the binary makes the estimation of binary evolution a three-body problem (M_x , M_c , and the lost mass δM), rendering a general solution difficult. Therefore, certain physically motivated scenarios for loss of mass from the binary (mass-loss modes) causing \dot{J}_{orb} viz., Jeans' mode, isotropic re-emission mode and intermediate mode (see Huang 1963 and van den Heuvel 1994) are usually explored. If the mass-loss from the binary is the most dominant factor contributing to \dot{J}_{orb} , assuming a mass-loss to proceed in any of these three mentioned modes, \dot{J} can be expressed as (equation 16.18 in Tauris & Van Den Heuvel 2006):

$$\frac{\dot{J}}{J} = \frac{\alpha + \beta q^2 + \delta \gamma (1 + q^2) \dot{M}_c}{1 + q} \frac{\dot{M}_c}{M_c} \quad (3)$$

$$\dot{M}_x = -(1 - \alpha - \beta - \delta) \dot{M}_c \quad (4)$$

where α , β , and δ denote the fractions of mass lost from the companion by (i) direct isotropic wind without gravitationally interacting with the NS (Jean's mode), (ii) isotropic ejection after being captured by the NS gravitational field (Isotropic re-emission), and (iii) lost mass overcoming the individual gravitational attractions of companion and NS, and escape through the lagrangian points L_2 or L_3 to form an extended circumbinary ring revolving around the common mass ($M_c + M_x$) of binary at a radius of $\gamma^2 a_x$ (Intermediate mode), respectively. $q = M_c / M_x$ is the mass ratio and $\epsilon = 1 - \alpha - \beta - \delta$ denotes the fraction of mass accreted.

Individual contributions to orbital evolution from these three different modes of mass loss could be explored by assigning values for α , β , and δ and using the equations (2)–(4), assuming $\dot{e} = 0$.

A direct isotropic wind loss from the companion could be defined by ($\alpha = 1$, $\beta = \delta = 0$). If the lost mass has an outward velocity greater than the escape velocity, it emulates an instant reduction of the total mass in the binary and hence the gravitational attraction between two stellar components. This leads to expansion of the orbit ($\dot{P}_{\text{orb}} > 0$) instead of the observed orbital decay. Simulations of the wind loss from Wray 15–977 indeed show this physical scenario causing expansion of the orbit in GX 301–2 (fig. 5 of Bunzel et al. 2023).

Isotropic re-emission from the vicinity of the NS could be defined by ($\alpha = 0$, $\beta = 1$, $\delta = 0$). In this case, the mass lost by the stellar wind from Wray 15–977 is first conservatively captured by the gravitational pull of NS and then re-ejected isotropically from the vicinity of NS. The re-emission of matter could occur due to radiation/magnetically driven wind from the neutron star as pointed out by Doroshenko et al. (2010). This scenario can lead to orbital decay. Substituting known values from Table 3 demonstrates that the orbital decay observed in GX 301–2 can occur for $\dot{M}_c \sim 9 \times 10^{-6} M_\odot \text{ yr}^{-1}$. Despite the scenario being considered, it cannot fully account for the observed orbital evolution in GX 301–2 because of the companion’s inability to undergo a conservative mass transfer to the NS vicinity due to the poor wind capture efficiency ($e_{\text{wind}} < 1$).

Anisotropic mass-loss from the companion through L_2 or L_3 resulting in the formation of an extended toroidal ring around the common mass ($M_c + M_x$) at a distance $\gamma^2 a_x$ from the centre of mass could be defined by ($\alpha = \beta = 0$, $\delta = 1$). For $\gamma \gtrsim 1$, $\dot{M}_c \leq 9 \times 10^{-6} M_\odot \text{ yr}^{-1}$ have the potential to produce the observed orbital decay in GX 301–2.

Although each mass loss mode alone could not be responsible for the observed orbital decay, it is possible that the actual mass ejection mode could be a composite of these idealized modes, and thereby produce the observed orbital decay.

4.2.3 Tidal interaction

Apart from mass-loss from the binary, another dominant mechanism that can contribute to \dot{J}_{orb} is tidal interaction between the NS and the rotating deformable companion in an eccentric binary (Darwin 1879; Lecar, Wheeler & McKee 1976). The compact object raises a tide on the surface of the companion. The tide facilitates angular momentum exchange between the rotating companion and the binary orbit and the dissipation of rotational and orbital energies. This results in synchronising the rotation of the companion and binary orbit (tidal synchronization) and circularizing the binary orbit (tidal circularization). If the companion rotation frequency (Ω_c) is less than the binary orbital frequency (Ω_{orb}), the retarding force of tide at the periastron is expected to circularize the orbit and cause orbital decay in the process.³ The spin angular momentum of the companion will increase at the expense of orbital angular momentum in this scenario.

A general form of tidal evolution in an HMXB is rather complex, which includes invoking dynamical tides that cause oscillating tidal response from the companion (Witte & Savonije 1999). However, a fairly simple approximation is the weak friction model of the tide which does not include the non-linear tidal dissipation processes (Refer Hut 1981). Our objective is to comprehend the swift orbital evolution witnessed in GX 301–2 concerning tidal dissipation through the weak friction model. Calculations based on Lecar, Wheeler & McKee (1976) and Hut (1981) under the assumption of weak friction model shows that tidal dissipation in the outer convective envelope of Wray 15–977 having a characteristic $\lambda \eta v_{\text{conv}} = 2 \times 10^{-4} \text{ km s}^{-1}$ (λ is the fractional depth of the convective layer of the companion, η is the fractional mass of the convective layer, and v_{conv} is the convective velocity) can cause the observed orbital decay in GX 301–2 (see Appendix D for detailed calculation). Considering the significant mass loss rate of the companion which can cause expansion of the binary orbit, the calculated convective

envelope parameters would be a lower limit if tidal dissipation is the lone factor driving orbital decay in GX 301–2.

A complete consideration of the effect of tidal interaction invoking the dynamical tides to estimate the tidal parameters required to produce the observed rapid orbital evolution of GX 301–2 is beyond the scope of this work. However, we refer to the work of Lai (1996) which discusses the orbital decay of the young eccentric binary radio pulsar PSR J0045–7319 having similar binary parameters as GX 301–2 ($P_{\text{orb}} \sim 52 \text{ d}$, $e \sim 0.8$, B-type $M_c \sim 9 M_\odot$, $a_x \sim 12 R_\odot$) and exhibits a rapid orbital decay of $|P_{\text{orb}}/\dot{P}_{\text{orb}}| \sim 5 \times 10^5 \text{ yr}$. Lai (1996) had shown that tidal interaction between the pulsar and a retrograde spinning companion may cause such a rapid orbital decay by invoking dynamical tides.

In binary systems such as GX 301–2, where there exists a significant difference in the mass of the components, with the mass ratio $M_c/M_x \sim 35$, it is possible for the system to undergo a Common Envelope (CE) phase during the later stages of evolution, due to either tidally induced orbital decay or significant Roche lobe overflow. Tidal interactions proceed towards synchronizing the slow rotation of the companion star with the fast binary orbit. However, in situations where the companion star is significantly more massive than the neutron star, the latter finds it difficult to spin up the former. An intriguing outcome occurs when $J_{\text{orb}} \lesssim 3J_c$ (equations 102 and 99 in van den Heuvel 1994), where the binary orbit continues to shrink, gradually achieving synchronization with the slowly spinning, massive companion, culminating in ‘tidal catastrophe’ where the neutron star spirals towards the core of the companion and merges.

Assuming an optimal scenario in which the binary orbit synchronises with the companion by the time of circularization, i.e. $\Omega_c = \Omega_{\text{orb}} = \Omega$. The relation $3J_c/J_{\text{orb}} > 1$ can be simplified to $3I_c/I_{\text{orb}} > 1$ (see Lecar, Wheeler & McKee 1976), where I_c and I_{orb} represents the moment of inertia of the companion and binary orbit, respectively, at the later circularized phase. Since the orbital separation is expected to shrink by this time, $I_{\text{orb}} \lesssim M_x a_x^2 \lesssim 4.4 \times 10^4 M_\odot R_\odot^2$. Meanwhile, the companion star is expected to evolve, resulting in an increase in its radius and a decrease in mass due to stellar wind. Assuming $I_c \approx M_c R_c^2 \approx 40 \times 10^4 M_\odot R_\odot^2$. The ratio $3I_c/I_{\text{orb}}$ is $\gtrsim 30$, indicating an unstable orbit post orbit circularization and the possibility of tidal catastrophe.

In the Roche lobe overflow phase, if the NS cannot accept the Roche lobe overflowed matter from the companion beyond the Eddington accretion rate, it forms a CE surrounding both stars. This CE phase can also result in the spiral in of NS due to frictional drag in the companion’s stellar envelope, as proposed by Bunzel et al. (2023) for GX 301–2. The aftereffect of the CE phase could be the ejection of the common envelope and subsequent formation of a binary comprising the already existing neutron star and the companion’s He-rich core. However, if the orbital energy lost during spiralling-in is not efficiently converted into mechanical energy and transferred to the envelope for CE ejection, it may instead result in the NS merging with the core of the companion. The resulting unique object has an NS core surrounded by H/He envelope (van den Heuvel 1994) and is called Thorne–Żytkow Object (TZO) (Thorne & Żytkow 1977). The same may happen with the Tidal catastrophe as well. GX 301–2 is thus a prospective future TZO candidate.

5 CONCLUSIONS

In this study, we utilized the recurring pre-periastron flares observed in the long-term X-ray light curves of GX 301–2 to investigate its orbital period evolution. Our analysis yielded a measured orbital

³One could grasp in a general sense the tide induced orbital decay, based on the principle of Hohmann orbit for satellite transfer (Hohmann 1960), even though both phenomena are unrelated.

decay time-scale of $|\dot{P}_{\text{orb}}/P_{\text{orb}}| \sim 2 \times 10^{-5} \text{ yr}^{-1}$, which is currently the shortest known evolution timescale for an HMXB. Previous estimates of this decay time-scale were based on pulse TOA analysis, which is influenced by the large orbital intensity variations and spin-up/down fluctuations of the pulsar. Our analysis of the long-term light curves, however, relies on the recurring orbital intensity profile, which is independent of the pulse TOA methods. There is a difference of about a factor of two between our estimate and the previous estimate based on pulse TOA analysis. Our estimate is limited by the repeatability of pre-periastron flares and is dependent on the stability and recurrence of the process causing these flares, which is still uncertain. We argue that a combination of distinct mechanisms, such as unique mass loss pathways and/or tidal interaction could be driving this rapid orbital decay.

ACKNOWLEDGEMENTS

We acknowledge the use of public data from the Swift data archive. This research has made use of MAXI data provided by RIKEN, JAXA, and the MAXI team. This research has made use of data and/or software provided by the High Energy Astrophysics Science Archive Research Center (HEASARC), which is a service of the Astrophysics Science Division at NASA/GSFC. We acknowledge the use of quick-look results provided by the ASM/RXTE team. We thank the anonymous referee for helpful suggestions.

DATA AVAILABILITY

All the data underlying this research article are publicly available for download from the respective mission web pages.

REFERENCES

- Bachetti M. et al., 2022, *ApJ*, 937, 125
 Barthelmy S. D. et al., 2005, *Space Sci. Rev.*, 120, 143
 Boldin P. A., Tsygankov S. S., Lutovinov A. A., 2013, *Astron. Lett.*, 39, 375
 Bunzel A. S., García F., Combi J. A., Chaty S., 2023, *A&A*, 670, A80
 Clark J. S., Najarro F., Negueruela I., Ritchie B. W., Urbaneja M. A., Howarth I. D., 2012, *A&A*, 541, A145
 Darwin G. H., 1879, *The Observatory*, 3, 79
 Doroshenko V., Santangelo A., Suleimanov V., Kreykenbohm I., Staubert R., Ferrigno C., Klochov D., 2010, *A&A*, 515, A10
 Eggleton P., 2006, *Evolutionary Processes in Binary and Multiple Stars* Cambridge University Press,
 Fürst F. et al., 2018, *A&A*, 620, A153
 Gehrels N. et al., 2004, *ApJ*, 611, 1005
 Haberl F., 1991, *ApJ*, 376, 245
 Hemphill P. B. et al., 2019, *ApJ*, 873, 62
 Hohmann W., 1960, *The Attainability of Heavenly Bodies*, National Aeronautics and Space Administration, United States
 Huang S.-S., 1963, *ApJ*, 138, 471
 Hut P., 1981, *A&A*, 99, 126
 Islam N., Paul B., 2014, *MNRAS*, 441, 2539
 Islam N., Paul B., 2016, *MNRAS*, 461, 816
 Jahoda K., Swank J. H., Giles A. B., Stark M. J., Strohmayer T., Zhang W., Morgan E. H., 1996, in Siegmund O. H., Gummin M. A. eds, *Proc. SPIE Conf. Ser. Vol. 2808, EUV, X-Ray, and Gamma-Ray Instrumentation for Astronomy VII*. SPIE, Bellingham, p. 59
 Jenke P. A., Finger M. H., Wilson-Hodge C. A., Camero-Arranz A., 2012, *ApJ*, 759, 124
 Kaper L., Lamers H. J. G. L. M., Ruymaekers E., van den Heuvel E. P. J., Zuiderwijk E. J., 1995, *A&A*, 300, 446
 Klis M., Bonnet-Bidaud J., 1984, *A&A*, 135, 155
 Koh D. T. et al., 1997, *ApJ*, 479, 933
 Lai D., 1996, *ApJ*, 466, L35
 Leahy D. A., 1987, *A&A*, 180, 275
 Leahy D. A., Kostka M., 2008, *MNRAS*, 384, 747
 Lecar M., Wheeler J. C., McKee C. F., 1976, *ApJ*, 205, 556
 Levine A. M., Bradt H., Cui W., Jernigan J. G., Morgan E. H., Remillard R., Shirey R. E., Smith D. A., 1996, *ApJ*, 469, L33
 Liu J., 2020, *MNRAS*, 496, 3991
 Lutovinov A., Tsygankov S., Chernyakova M., 2012, *MNRAS*, 423, 1978
 Malacaria C., Jenke P., Roberts O. J., Wilson-Hodge C. A., Cleveland W. H., Mailyan B., 2020, *ApJ*, 896, 90
 Manikantan H., Paul B., Roy K., Rana V., 2023, *MNRAS*, 520, 1411
 Matsuoka M. et al., 2009, *PASJ*, 61, 999
 Meegan C. A., Fishman G. J., Wilson R. B., Paciesas W. S., Pendleton G. N., Horack J. M., Brock M. N., Kouveliotou C., 1992, *Nature*, 355, 143
 Mihara T. et al., 2011, *PASJ*, 63, S623
 Mönkkönen J., Doroshenko V., Tsygankov S. S., Nabizadeh A., Abolmasov P., Poutanen J., 2020, *MNRAS*, 494, 2178
 Mukherjee U., Paul B., 2003, *Bull. Astron. Soc. India*, 31
 Nagase F. et al., 1982, *ApJ*, 263, 814
 Naik S., Paul B., 2004, *ApJ*, 600, 351
 Parkes G. E., Mason K. O., Murrin P. G., Culhane J. L., 1980, *MNRAS*, 191, 547
 Paul B., 2017, *J. Astrophys. Astron.*, 38, 39
 Paul B., Naik S., 2011, *Bull. Astr. Soc. India*, 39, 429–449 (arXiv:1110.4446)
 Pravdo S. H., Ghosh P., 2001, *ApJ*, 554, 383
 Raichur H., Paul B., 2010, *MNRAS*, 401, 1532
 Raman G., Varun B., Paul B., Bhattacharya D., 2021, *MNRAS*, 508, 5578
 Sato N., Nagase F., Kawai N., Kelley R. L., Rappaport S., White N. E., 1986, *ApJ*, 304, 241
 Shirke P., Bala S., Roy J., Bhattacharya D., 2021, *J. Astrophys. Astron.*, 42, 58
 Singh N. S., Naik S., Paul B., Agrawal P. C., Rao A. R., Singh K. Y., 2002, *A&A*, 392, 161
 Tauris T., Van Den Heuvel E., 2006, *Formation and Evolution Of Compact Stellar X-ray Sources*, Walter Lewin M. Van der Klis, Cambridge University Press, 623–666
 Thorne K. S., Zytkov A., 1977, *ApJ*, 212, 832
 Witte M. G., Savonije G. J., 1999, *A&A*, 350, 129
 van den Heuvel E. P. J., 1994, in *Saas-Fee Advanced Course 22: Interacting Binaries*. Springer Berlin, Heidelberg, p. 263

APPENDIX A: ERROR ESTIMATION BY BOOTSTRAP

(i) In each of the dwell light curves used, count-rate in the i^{th} temporal bin c_i was replaced with $c_i + x\sigma_i$, where x was independently randomly sampled from the uniform distribution $\mathcal{U}(-1, 1)$ (see Lutovinov, Tsygankov & Chernyakova 2012; Boldin, Tsygankov & Lutovinov 2013; Raman et al. 2021).

(ii) Using this technique, 1000 sample light curves were simulated for each long-term light curve and pulsed flux history.

(iii) The best period from each simulated light curve was estimated by fitting a Gaussian to the χ^2 versus P_{orb} plot and retrieving the best-fitting Gaussian centre.

(iv) The mean (μ) and standard deviation (σ) of the distribution of best-fitting Gaussian centres for 1000 simulations from each light curve were assigned its P_{orb} and ΔP_{orb} , respectively.

APPENDIX B: ENERGY DEPENDENCE OF FLARES

To assess the energy dependence of the arrival time of pre-periastron flares, we used the overlapping duration of *Swift*/BAT (15–50 keV) light curve with *RXTE*/ASM (1.5–12 keV), *MAXI* (2–20, 2–4, 4–10, and 10–20 keV) and *Fermi*/GBM (12–50 keV; Fig. 4), and the overlapping duration of *RXTE*/ASM with *CGRO*/BATSE. BAT and BATSE were selected as reference light curves, and the below steps were performed individually for both.

(i) The overlapping duration between lc_{ref} and each lc_{oth} s were first identified, where lc_{ref} is the reference light curve (BAT or BATSE) and lc_{oth} is the other light curve having an overlap with lc_{ref} .

(ii) XRONOS compatible window files were created using the HEASOFT tool *xronwin* to restrict data to the overlap duration.

(iii) In the overlap duration, lc_{ref} and lc_{oth} were folded at an arbitrary reference epoch (T_{fold}) with the average of the orbital periods (P_{orb}) derived from the two light curves (Table 1).

(iv) The vicinity of the flare in each folded orbital intensity profile was modelled with a constant + lorentzian and the centre of lorentzian was estimated along with its 2.7σ error. The centre of lorentzian is assigned as the phase of flare peak (ϕ_{flare}).

(v) Number of orbits elapsed since T_{fold} to the middle of each window (N) was estimated by $\text{floor}((T_{\text{window-mid}} - T_{\text{fold}})/P_{\text{orb}})$. Flare time for i^{th} light curve was estimated by $T_{\text{flare}, i} = T_{\text{fold}} + NP_{\text{orb}, i} + P_{\text{orb}, i}\phi_{\text{peak}, i}$.

(vi) The delay (ΔT_{flare}) between the flare times of the reference light curve and the other light curve was calculated (Table 2).

APPENDIX C: ORBITAL PERIOD DERIVATIVE FROM TIMING SIGNATURE OF THE PRE-PERIASTRON FLARES

The pulsed histories from BATSE (20–50 keV) and GBM (12–50 keV), and the long-term light curves from ASM (1.5–12 keV), BAT (15–50 keV), and MAXI (10–20 keV) were used to estimate the time signature of flare peaks. The steps were followed in the order in which they are listed below:

(i) Each light curve was split into three equal slices (windows) and was folded with the respective orbital period (Table 1) at the epoch corresponding to the beginning of the window. The idea is to find three representative flare-peak times per light curve.

(ii) The maximum SNR for orbital intensity profile was obtained from BAT, where it was also found that lorentzian is a better

fit to the flare compared to Gaussian based on weighted variance. Therefore, a constant + lorentzian was fit on the folded light curve in the vicinity of flare (ϕ_{orb}), and the centre of the best fit lorentzian was assigned the phase of flare peak $\phi_{\text{flare}} \pm \Delta\phi_{\text{flare}}$.

(iii) Orbital cycles n elapsed since the start of the window ($T_{\text{win-begin}}$) to the flare peak (T_{flare}) in each slice of the light curve was estimated by $\text{floor}((T_{\text{slice-mid}} - T_{\text{win-begin}})/P_{\text{orb}})$. The flare time was then estimated by $T_{\text{flare}} = T_{\text{win-begin}} + nP_{\text{orb}} + \phi_{\text{peak}}P_{\text{orb}}$.

(iv) The data T_{flare} versus n was fitted with a linear function, and the residuals to the best-fitting linear function were then checked for a quadratic trend indicative of orbital evolution.

APPENDIX D: TIDAL EVOLUTION

Under the weak friction model approximation, due to the internal frictional properties of the companion, the formation of a tidal bulge occurs τ s after the compact object exerts gravitational force to raise it. τ is called the tidal time lag and by this duration, the compact object would have moved a relative angular displacement of $\delta = \tau\sigma$ about the tidal bulge, called the tidal lag angle. This displacement of the tidal bulge relative to the line connecting two stars results in a tidal torque that affects the binary orbit. The tidal time lag (τ) is related to the properties of stellar structure. The degree of response of the binary orbit to the tidal forces is represented by the apsidal motion constant k . $\sigma \approx \Omega_c - \Omega_{\text{orb}}$ is the apparent angular velocity of NS relative to the surface of the companion.

The rate of change of the semimajor axis due to tidal circularization of the binary is given by Hut (1981) as the following equation (D1):

$$\frac{\dot{a}}{a} = \frac{2\dot{P}_{\text{orb}}}{3P_{\text{orb}}} = -6\frac{k}{T}\dot{q}(1+\dot{q})\left(\frac{R_c}{a}\right)^8 \frac{1}{(1-e^2)^{7.5}} \times \left[f_1(e^2) - (1-e^2)^{1.5} f_2(e^2) \frac{\Omega_c}{n} \right], \quad (\text{D1})$$

where, a and P_{orb} are the semimajor axis and orbital period, and \dot{a} and \dot{P}_{orb} their rate of changes, R_c is the companion radius, e is the binary eccentricity, Ω_c is the rotation frequency of the companion. After substituting the known parameters of GX 301–2 from (Table 3),

$$f_1(e^2) = 1 + \frac{31}{2}e^2 + \frac{255}{8}e^4 + \frac{185}{16}e^6 + \frac{25}{64}e^8 \sim 6.1$$

$$f_2(e^2) = 1 + \frac{15}{2}e^2 + \frac{45}{8}e^4 + \frac{5}{16}e^6 \sim 2.9$$

$$n = \sqrt{\frac{G(M_x + M_c)}{a_x^3}} \sim 1.9 \times 10^{-6} \text{ rad s}^{-1}$$

$$\Omega_c = \frac{2\pi}{P_c} \sim 1.01 \times 10^{-6} \text{ rad s}^{-1}$$

$$\dot{q} = \frac{M_x}{M_c} \sim 0.03$$

$$T = \frac{R_c^3}{GM_c\tau} \sim \frac{3.3 \times 10^{10}}{\tau} \text{ s.}$$

Substituting in equation (D1)

$$-\frac{2 \times 5.52 \times 10^{-13}}{3} \approx -6 \frac{k\tau}{3.3 \times 10^{10}} \times 0.029 \times 0.003 \times 6.5 \times 5.05$$

$$k\tau \approx 0.64 \text{ s}$$

If tidal dissipation is assumed to be facilitated by an outer convective layer around the stellar core of Wray 15–977, equation (A1) in Lecar, Wheeler & McKee (1976) gives the relation of $k\tau$ to the

characteristics of such a convection layer as

$$k\tau \approx 25 \text{ s} \frac{\lambda\eta v_{\text{conv}} (\text{km s}^{-1})}{(g/g_{\odot})}, \quad (\text{D2})$$

where, λ (fractional depth of convective layer), η (fractional mass of the convective zone), and v_{conv} (convective velocity) define the property of the convective envelope, and

$$\frac{g}{g_{\odot}} = \frac{(M_c/M_{\odot})}{(R_c/R_{\odot})^2} \approx 0.007.$$

Substituting $k\tau = 0.71 \text{ s}$ in equation (D2) gives

$$\lambda\eta v_{\text{conv}} \approx 1.68 \times 10^{-4} \text{ km s}^{-1}.$$

APPENDIX E: O–C CURVE WITHOUT CORRECTING FOR ENERGY DEPENDENCE OF FLARES

When the energy dependence of the pre-periastron flares were not taken into account for generating the O–C curve as opposed to the analysis described in Section 3.3, a quadratic fit on the resulting O–C curve yielded a best fit $\dot{P}_{\text{orb}} = -2.3 \times 10^{-6} \text{ s s}^{-1}$ with a very large wvar of 965 for 13 d.o.f (Fig. E1).

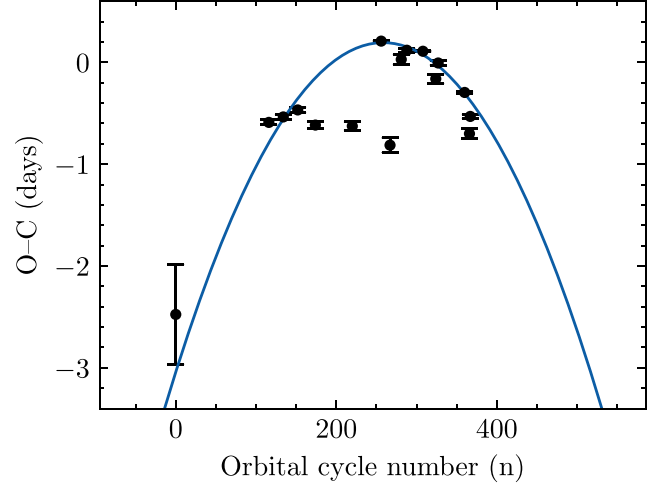


Figure E1. Results of fitting a quadratic function on the O–C curve that was generated without correcting for the energy dependence of the pre-periastron flares. The fit returned a best fit $\dot{P}_{\text{orb}} = -2.3 \times 10^{-6} \text{ s s}^{-1}$, albeit with a very large fit statistic.

This paper has been typeset from a $\text{\TeX}/\text{\LaTeX}$ file prepared by the author.